

Non-Aqueous Approach to Synthesize Amorphous/Crystalline Metal Oxide-Graphene Nanosheet Hybrid Composites

Xiangbo Meng, Dongsheng Geng, Jian Liu, Mohammad Norouzi Banis, Yong Zhang, Ruying Li, and Xueliang Sun*

Department of Mechanical and Materials Engineering, The University of Western Ontario, London, Ontario N6A 5B8, Canada

Received: June 24, 2010; Revised Manuscript Received: September 10, 2010

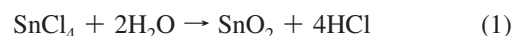
Presently, there is a dramatically increasing interest in developing graphene-supported nanocomposites, due to their unprecedented properties. Apart from the methods exposed in previous studies, this work presents a nonaqueous approach of using atomic layer deposition (ALD) to constitute novel metal oxide-graphene hybrid nanocomposites based on graphene nanosheet (GNS) powders. It is demonstrated that this gas–solid strategy exhibits many unique benefits. It reports for the first time that the as-prepared SnO₂-GNS nanocomposites are featured with not only tunable morphologies but controllable amorphous and crystalline phases of SnO₂ component as well, using SnCl₄ and H₂O as the ALD precursors. Furthermore, the determinant factors and underlying mechanisms were outlined and discussed in this work. As a consequence, besides the demonstration of ALD as an important approach for nanoarchitecturing novel metal oxide-GNS composites, the as-synthesized SnO₂-GNS hybrid nanocomposites provide more choices for many important applications, such as lithium-ion batteries, solar cells, and gas sensing.

1. Introduction

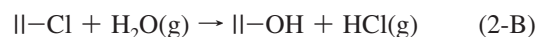
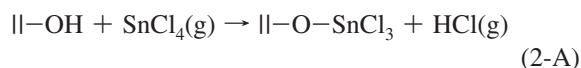
Interest in nanocomposites is ever-growing, ascribed to their peculiarities in combining desirable properties of hybrid nanosized building blocks for a given application. In this way, carbon nanotubes (CNTs), being excellent one-dimensional (1D) candidates, have been extensively incorporated in a wide range of nanocomposites for many applications.^{1–4} Presently, following CNTs, graphene being a 2D nanoscale building block is attracting more and more effort toward developing novel nanoarchitectured composites since its discovery⁵ in 2004. To date, graphene (or graphene stacks, a few layers of graphene) has been reported to incorporate with three main types of materials: polymers,^{6–9} metals,^{10–13} and metal oxides,^{14–20} covering a series of applications (including field emitters, photocatalysis, conductors, supercapacitors, fuel cells, and batteries, etc.) with improved mechanical, electrical, optical, or electrochemical properties. For metal oxide-graphene nanocomposites (MO-GNCs), however, only limited cases were exposed in literature and they were prominently synthesized in aqueous solutions via two routes: wet chemical deposition,^{15–19} and solution-based mechanical mixing.²⁰ The former route was generally carried out with a complicated and tedious process, accounting for several tens of hours.^{15–19} As an alternative, the latter one was simply performed through mechanically mixing available metal oxide nanoparticles with graphene dispersions,²⁰ having less manipulation on metal oxide nanoparticles and thereby lacking of flexibility and precision as a synthesis strategy. Commonly, the aqueous solution-based methods exposed in literature show inability to precisely control the morphologies and structures of metal oxides.

With attempts to circumvent the above-mentioned issues, recently we successfully fulfilled the synthesis of MO-GNCs via a nonaqueous approach and the first case will be reported

in this work. This strategy is featured by applying the technique of atomic layer deposition (ALD) to deposit metal oxides on graphene nanosheet (GNS) powders. Our studies demonstrated that this approach can provide a precise fabrication of MO-GNCs with more benefits, opening a potential avenue for mass production. Characteristically, ALD is a surface-controlled gas–solid process and uniquely performed by two sequentially cyclic half-reactions.²¹ In comparison to wet chemical routes as well as traditional chemical and physical vapor deposition, ALD contributes to a controllable, uniform, and conformal deposition at the atomic level,²¹ and is going into a fashion in nanotechnology to synthesize novel nanostructures and nano-devices.^{22,23} In addition, ALD has the capability to deposit both inorganic (metals and metal oxides)²⁴ and organic materials (polymers).²¹ In the case of SnO₂, it has mainly been performed on flat substrates (e.g., quartz glass) via ALD^{25–27} using SnCl₄ and H₂O as well as other precursors. The reaction between SnCl₄ and H₂O is fairly straightforward with the product of SnO₂, as described in the following Reaction 1.



In the ALD of SnO₂ (ALD-SnO₂), however, Reaction 1 was replaced with two sequential half-reactions as suggested by the following:²⁸



where the symbol || denotes the substrate surface, and (g) refers to gas phase species. One “A” pulse of SnCl₄ (Reaction 2-A) and one following “B” pulse of H₂O (Reaction 2-B) consist of

* To whom correspondence should be addressed. E-mail: xsun@eng.uwo.ca.

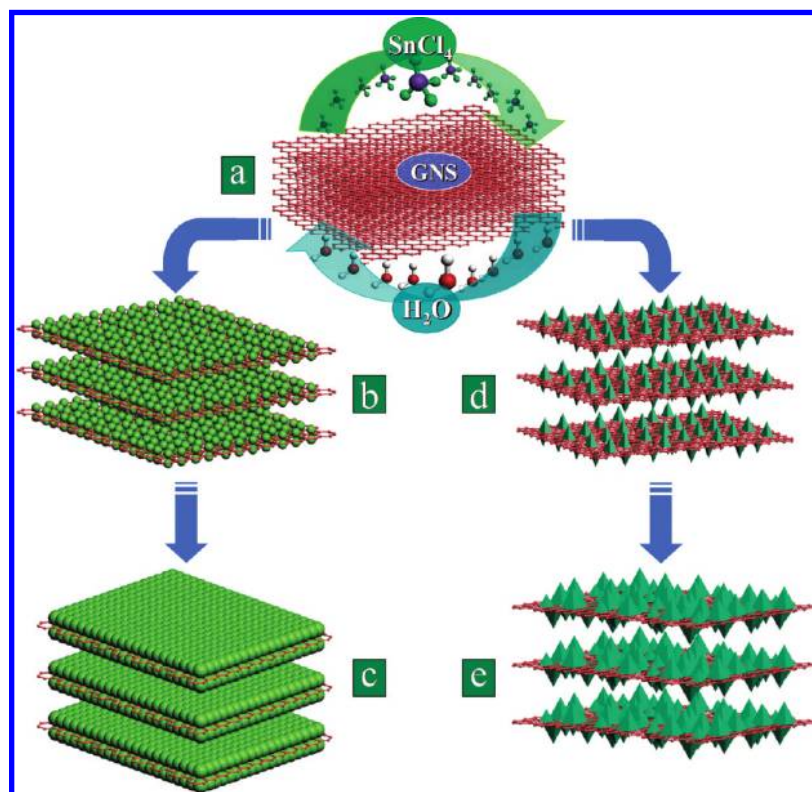


Figure 1. Schematic illustration of the precise approach to tune the morphology and amorphous–crystalline phases via atomic layer deposition technique (ALD). (a) ALD-SnO₂ process employed on graphene nanosheets (GNS) using SnCl₄ and H₂O as the two precursors to form amorphous/crystalline SnO₂-GNS nanocomposites; (b) uniformly distributed amorphous SnO₂ nanoparticles on GNS surface; and (c) amorphous SnO₂ thin film formed on GNS surface by growing nanoparticles; (d) small crystalline SnO₂ nanoparticles uniformly distributed on GNS surface; and (e) large SnO₂ nanoparticles uniformly distributed on GNS surface with higher density.

one typical “A-B” cycle in ALD process, and the cycling of “A-B” half-reactions can build up SnO₂ films increasing with accuracy at the atomic level. In this work, we deduce this ALD strategy through exemplifying the synthesis of SnO₂-GNS composites, using SnCl₄ and H₂O as the ALD precursors.

The successful demonstration of ALD-SnO₂ on GNS produced 3-D nanoarchitected networks of SnO₂-GNS composites. More importantly, the composites are featured with tunable morphologies and controllable phases of the SnO₂ component. It was found that the SnO₂ component can present amorphous and crystalline phase through suitably adjusting the growth temperature. In addition, due to the cycling nature of ALD, the synthesis of SnO₂-GNS nanocomposites also showed a characteristic on precisely controlling the morphologies of as-deposited SnO₂. Thus, this work is significant with respect to three main outcomes: (i) ALD was for the first time suggested and successfully demonstrated as an efficient strategy to synthesize MO-GNCs; (2) the as-synthesized nanocomposites of SnO₂-GNS presented fine-tuned morphologies; and (3) well-controlled structural phases from amorphous to crystalline SnO₂. To highlight the outcomes from this nonaqueous approach, we used a schematic illustration to help readers understand, as shown in Figure 1. The ALD-SnO₂, as illustrated by Figure 1(a), is fulfilled by two sequential half reactions induced by SnCl₄ and H₂O, respectively. At a low growth temperature (200 °C), amorphous SnO₂ nanoparticles (Figure 1(b)) were uniformly formed on GNS in initial ALD cycles. The nanoparticles grew bigger and finally coalesced into a thin film (Figure 1(c)) with increased ALD cycles. At a high temperature (400 °C), however, crystalline SnO₂ nanoparticles were deposited on GNS and grew from small sizes (Figure 1(d)) to large ones (Figure 1(e)) with increased ALD cycles. Furthermore, the underlying mechanisms

responsible for controllable structural phases of SnO₂ were also explored in this work based on surface chemistry.

2. Experimental Section

2.1. Preparation of GNS. For preparation of GNS, we first oxidized natural graphite powder (45 μm, 99.99%, Sigma-Aldrich as shown in Figure SI-1(a) and (b), Supporting Information) using a modified Hummers method.²⁹ In detail, graphite powder (1 g) was first stirred in concentrated sulphuric acid (23 mL) with a following addition of sodium nitrate (0.5 g) at room temperature. The stirring lasted for 16 h, and then the mixture was cooled down to 0 °C. Thereafter, potassium permanganate (3 g) was added to form a new mixture. Two hours later, the mixture formed a green slurry around 35 °C, which was stirred for another 3 h. Then, water (46 mL) was slowly added into the paste with an increased temperature around 98 °C. The suspension was remained at this temperature for 30 min before it was further diluted with another addition of water and hydrogen peroxide (140 mL). In the following, the suspension was filtered and washed until the pH value of the filtrate was neutral. The as-received slurry is the so-called graphite oxide (GO, Figure SI-1(c) and (d), Supporting Information), which was further dried in a vacuum oven at 60 °C. To prepare GNS, the as-synthesized GO was first flushed by Ar for 20 min in a quartz tube. Then, the quartz tube was promptly moved into a Lindberg tube furnace with a preheated temperature around 1050 °C. After 30 s thermal treatment, GO was reduced into expanded GNS powders as illustrated in Figure 2(a).

2.2. ALD-SnO₂. The as-synthesized GNS powder was first loaded into a commercial ALD reactor (Savannah 100, Cambridge Nanotechnology Inc., USA) preheated to a preset growth

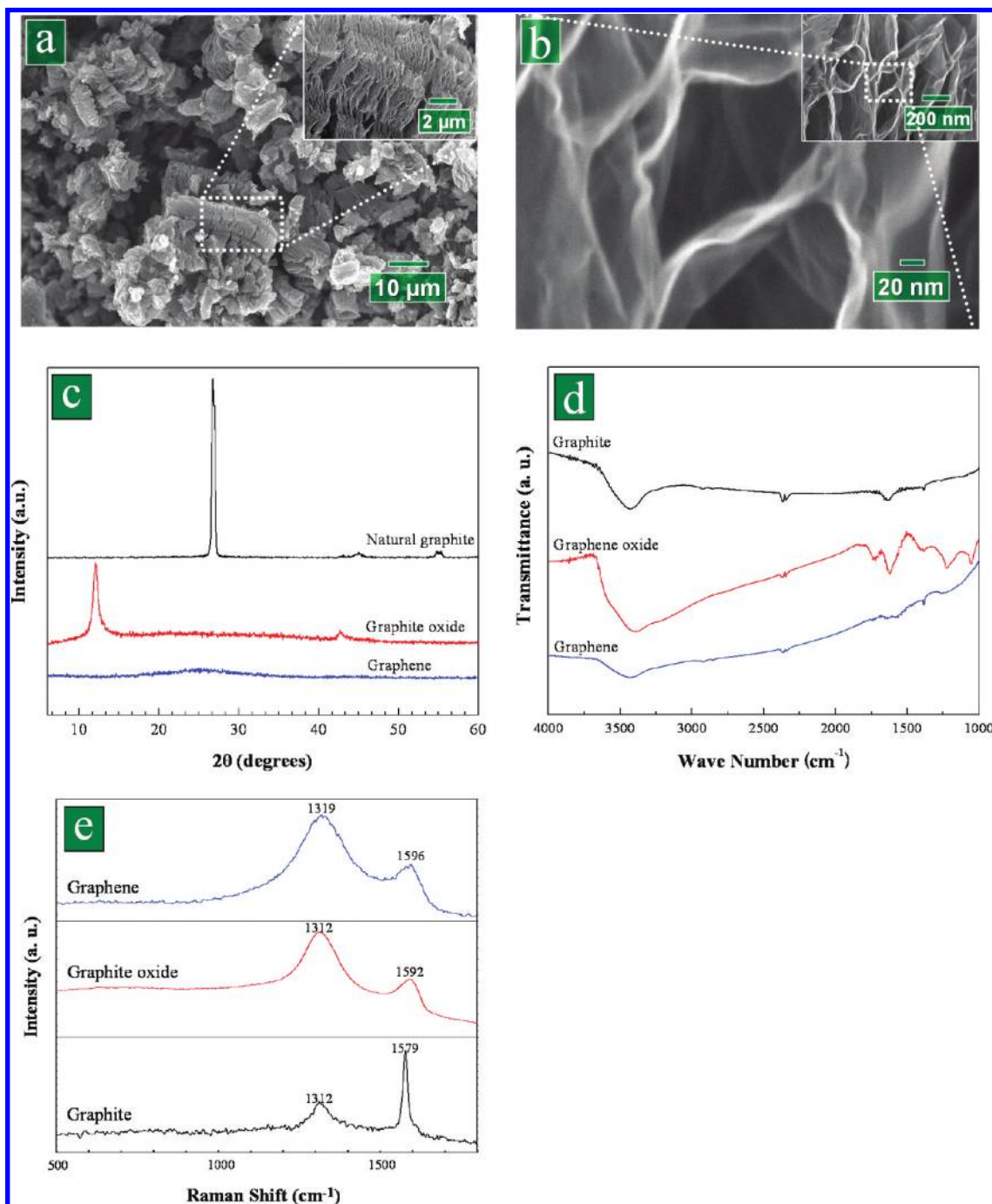


Figure 2. Characteristics of GNS: SEM images of (a) low magnification, and (b) high magnification; (c) XRD, (d) FTIR, and (e) Raman spectra.

temperature. In this study, two growth temperatures were applied, i.e., 200 and 400 °C. The following ALD-SnO₂ was performed through introducing tin(IV) chloride (99% SnCl₄, Sigma-Aldrich) and deionized water (DI H₂O) into the ALD reactor in an alternating manner. In the ALD processes, nitrogen was selected in this study as the carrier gas with a flow rate of 20 sccm, and the ALD reactor was sustained at a low level of pressure (typically 0.4 Torr) with a vacuum pump (Pascal 2005 I, Adixon). The ALD procedures were set as follows: (1) a 0.5 s supply of SnCl₄; (2) a 3 s extended exposure of SnCl₄ to GNS; (3) a 10 s purge of oversupplied SnCl₄ and any byproduct; (4) a 1 s supply of water vapor; (5) a 3 s extended exposure of water vapor to GNS; (6) a 10 s purge of oversupplied water and any byproduct. The aforementioned six-step sequence

constituted one ALD-SnO₂ cycle and the ALD processes were adjusted with different cycling numbers.

2.3. Characterization. To characterize our samples' morphologies, structures, and compositions, we used field emission scanning electron spectrometry (FE-SEM, Hitachi 4800S) coupled with energy dispersive spectroscopy (EDS), transmission electron microscope (TEM, Philips CM10), high-resolution transmission electron microscope (HRTEM, JEOL 2010 FEG), X-ray diffractometer (XRD, Inel multipurpose diffractometer), Raman spectrometry (RXN1-785, Kaiser Optical Systems InCo.), Fourier transform infrared spectroscopy (FTIR, Bruker Tensor 27), and the results are elucidated in the following sections.

3. Results and Discussions

The GNS powders employed in our study were made from natural graphite powders via a series of processes. During the preparation, graphite powders were first oxidized using Hummers method²⁹ with the product of graphite oxide (GO). Thereafter, GO was reduced via a rapid thermal expansion³⁰ which separated the layered GO into partially functionalized GNS. The as-synthesized GNS powders were characterized by SEM, XRD, FTIR, and Raman, as illustrated in Figure 2. In contrast to the natural graphite and GO (Figure SI-1, Supporting Information), the GNS powders (Figure 2(a) and insert) present a fluffy worm-like porous structure.³¹ The porous “worms” are featured by numerous honeycombs (inset of Figure 2(b)) surrounded by wrinkles of typically less than 3 nm in thickness (Figure 2(b)). XRD spectra patterns (Figure 2(c)) clearly distinguished the as-synthesized GNS from the natural graphite as well as GO. Graphite has the strongest (002) peak at 26.8° as well as three weak peaks of (100), (101), and (004) at 43°, 45°, and 55°, respectively. In comparison, GO shows a very strong (001) diffraction peak at 12°, suggesting that the interlayer distance increases and the structure is modified due to oxygenated groups,³² as well as a weak (100) diffraction peak around 43°. In contrast, the GNS received a broad diffraction (002) peak shifted back to 26.8°, implying that GO was reduced via the rapid thermal expansion and the extensive conjugated sp² carbon network (i.e., the ordered crystal structure) was restored.³³ FTIR spectra (Figure 2(d)) further clarified their differences in functional groups. It is easy to observe that the natural graphite mainly shows the stretching vibrations of hydroxyl (–OH) groups (3420 cm^{–1}) and C=C (1586 cm^{–1}), while GO has been added with the stretching vibrations of C=O (1736 cm^{–1}), carboxy C–O (1414 cm^{–1}), epoxy C–O (1220 cm^{–1}), and C–O (1100 cm^{–1}).^{34–36} In comparison, GNS mainly shows the stretching vibrations of hydroxyl (–OH) groups and C=C.^{34–36} The FTIR results imply that GNS was significantly reduced, and this is consistent to XRD results. Peaks below 900 cm^{–1} are usually not interpreted for they represent too complex a structural signature.³² Furthermore, the samples were examined by Raman spectroscopy, an essential tool to characterize graphene.³⁷ As illustrated in Figure 2(e), the Raman spectra underwent changes along the graphite-GO-GNS process, similar to those observed in the graphite to amorphous carbon transition.³⁸ The Raman spectra of the graphite show the in-phase vibration of the graphite lattice (G band) at 1579 cm^{–1} and a weak D band at 1312 cm^{–1}. The Raman spectra for GO present a broadened G band at 1592 cm^{–1}, owing to the presence of isolated double bonds that resonate at higher frequencies than the G band of graphite.³⁹ The D band of GO becomes evident and keeps at 1312 cm^{–1}, indicating the reduction in size of the in-plane sp² domains due to the extensive oxidation.⁴⁰ As for the Raman spectra of GNS, the G and D band are located at 1596 and 1319 cm^{–1}, respectively. Besides the similarities of Raman spectra between GO and GNS, it is noteworthy that the D/G intensity ratio of GNS (0.82) is, in comparison with the value (0.78) of graphite, increased, indicating a decrease in the size of the in-plane sp² domains and a partially ordered crystalline structure of GNS.³⁸

The GNS powders were thereafter used to prepare metal oxide-GNS nanocomposites via ALD-SnO₂ under different cycles. The samples after 300-cycle ALD-SnO₂ at 200 and 400 °C were characterized by XRD, and their XRD spectra were compared with those of the pristine GNS, illustrated in Figure 3(a). The XRD results show that, in comparison to the pristine GNS, the sample produced at 200 °C shows no observable

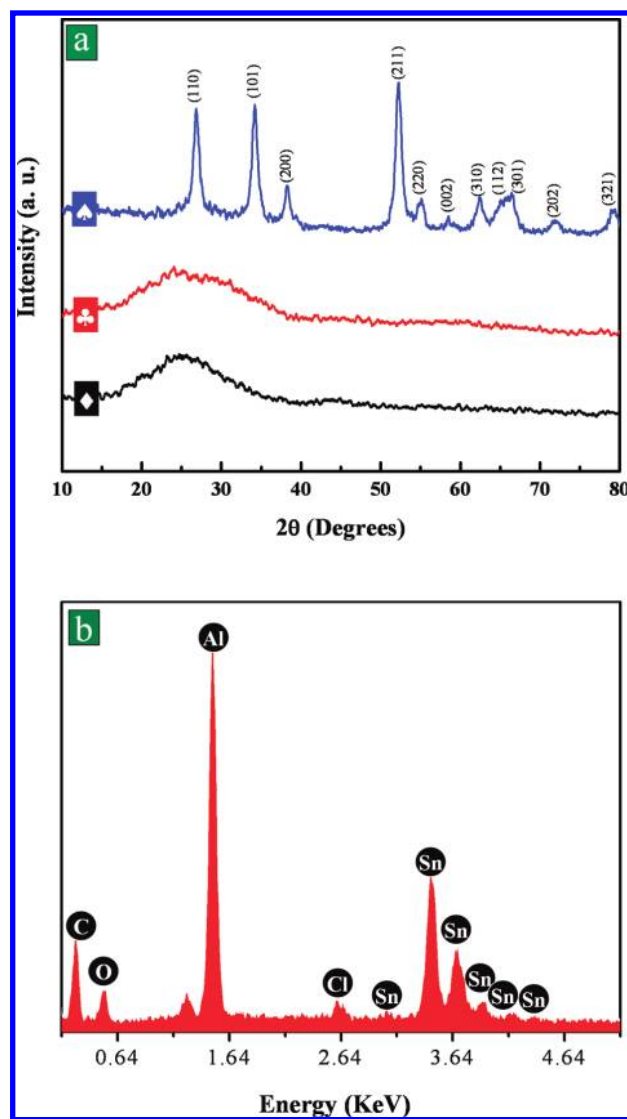


Figure 3. (a) XRD spectra of (diamond) GNS, (club) SnO₂-GNS nanocomposites synthesized at 200 °C, and (spade) SnO₂-GNS nanocomposites synthesized at 400 °C; (b) EDS spectra for SnO₂-GNS nanocomposites synthesized at 200 °C.

change while many characteristic peaks were with the sample produced at 400 °C. To confirm the formation of ALD-SnO₂ at 200 °C, the sample was examined by EDS equipped on FE-SEM, and EDS results (Figure 3(b)) revealed the presence of Sn, O, and C elements with the sample. The Al peak is resulted from the sample holder for EDS measurement. In addition, there is some Cl element resulting from unreacted functional groups. Thus, combined with the results disclosed by XRD, it was believed that amorphous SnO₂ has been deposited on GNS. Alternatively, the XRD peaks with the sample produced at 400 °C were identified in the standard card and consistent with those reference values of crystalline SnO₂ (Joint Committee on Powder Diffraction Standards (JCPDS) powder diffraction file (PDF) No. 41–1445). Thus, the ALD approach produced two different types of nanocomposites through simply adjusting growth temperatures: amorphous and crystalline SnO₂-GNS composites at 200 and 400 °C, respectively.

To further unveil the characteristics of the two types of nanocomposites produced at different temperatures, they were commonly examined by SEM and TEM. As shown in figure 4, ALD-SnO₂ on GNS at 200 °C was performed with various ALD cycles. The SEM image for 100 cycles of ALD-SnO₂ (Figure

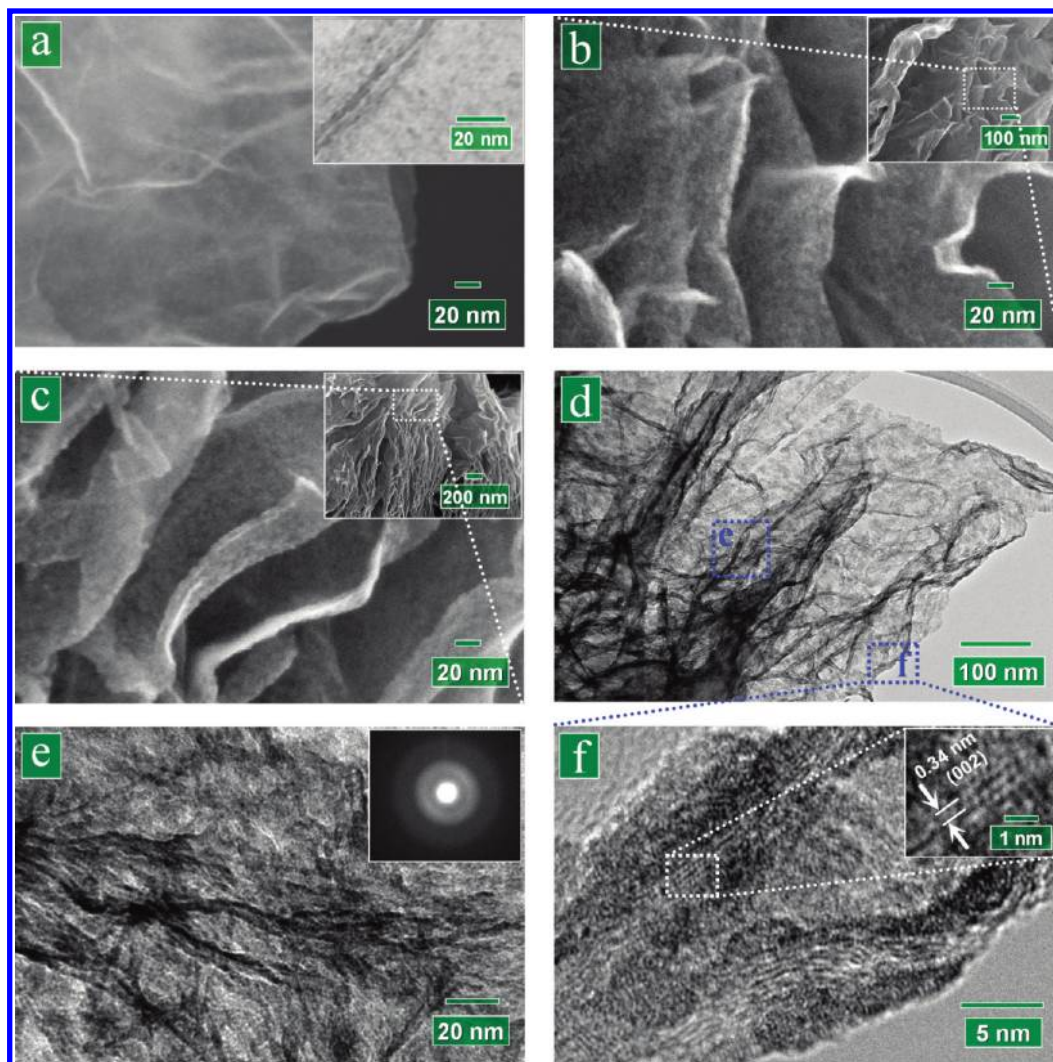


Figure 4. Amorphous SnO₂-GNS nanocomposites: (a) 100 ALD cycles of SnO₂; (b) 200 ALD cycles of SnO₂; (c) 300 ALD cycles of SnO₂; (d) low magnification TEM image of 300-cycle SnO₂; (e) and (f) HRTEM images of 300-cycle SnO₂.

4(a)) shows that GNS was covered with tiny nanoparticles (~ 3 nm, Figure SI-2(b), Supporting Information), which were confirmed by TEM (insert of Figure 4(a)). Upon 200 ALD cycles (Figure 4(b)), it was observed that GNS surface has been totally covered by SnO₂ nanoparticles (~ 5 nm, Figure SI-2(d), Supporting Information) of high density, and the as-synthesized SnO₂-GNS composite remains the porous structure. In the case of 300 ALD cycles, as shown in Figure 4(c) by SEM image, we observed a thin film formed on GNS. Obviously, the ALD-SnO₂ on GNS surface experienced an island-like growth in the first 200 ALD cycles at a growth temperature of 200 °C before the growing nanoparticles coalesced into a uniform layer. Additionally, it is also noteworthy that the ALD-SnO₂ was deposited equally on both sides of a single graphene (as disclosed in Figure 4, parts (b) and (c)). The sample after 300-cycle ALD-SnO₂ was further examined by TEM, as shown in Figure 4(d)–(f). We can observe from Figure 4(d) that the nanocomposite retains the morphologies of GNS with numerous wrinkles. In addition, two local areas, as blue-circled as “e” and “f”, were further shown in Figure 4(e),(f), respectively. With an increased magnification TEM image in figure 4(e), it is worth noting that GNS was uniformly coated, and selected area electron diffraction (SAED, insert of figure 4(e)) only shows the disordered nature of the composite. The HRTEM image in figure 4(f) further confirmed no crystalline structure with SnO₂,

but it is easy to observe the graphene stacked with 5–6 layers and the interlayer spacing keeps at 0.34 nm (insert of Figure 4(f)). On the basis of the above-discussed results, we can clearly conclude that amorphous SnO₂-GNS nanocomposites were synthesized at a growth temperature of 200 °C, exhibiting tunable morphologies of SnO₂ component and unchangeable morphologies of GNS.

Following the results of amorphous SnO₂-GNS nanocomposites prepared at 200 °C, the results of crystalline SnO₂-GNS nanocomposites prepared at 400 °C are shown in Figure 5. After an initial 100-cycle ALD-SnO₂, the sample in Figure 5(a) shows that GNS surface was deposited uniformly with numerous nanoparticles varying in the range from 10–20 nm. An averaging on 100 nanoparticles accounts for a value of ~ 13 nm for the nanoparticle size. Figure 5(b) shows nanoparticles growing bigger with an average size of ~ 27 nm after 200 ALD cycles, and Figure 5(c) shows ever-growing nanoparticles having an average size of ~ 33 nm after 300 ALD cycles. Thus, we observed a nonlinear growth with nanoparticles. In addition, it is noteworthy that, at each stage of different ALD cycles, there were always some tiny particles newly appeared and the density of nanoparticles showed an increasing tendency, implying that SnO₂ nanoparticles might not all nucleate at the same time. The underlying reason could be attributed to deficient exposure of some local surface areas to precursors during ALD processes,

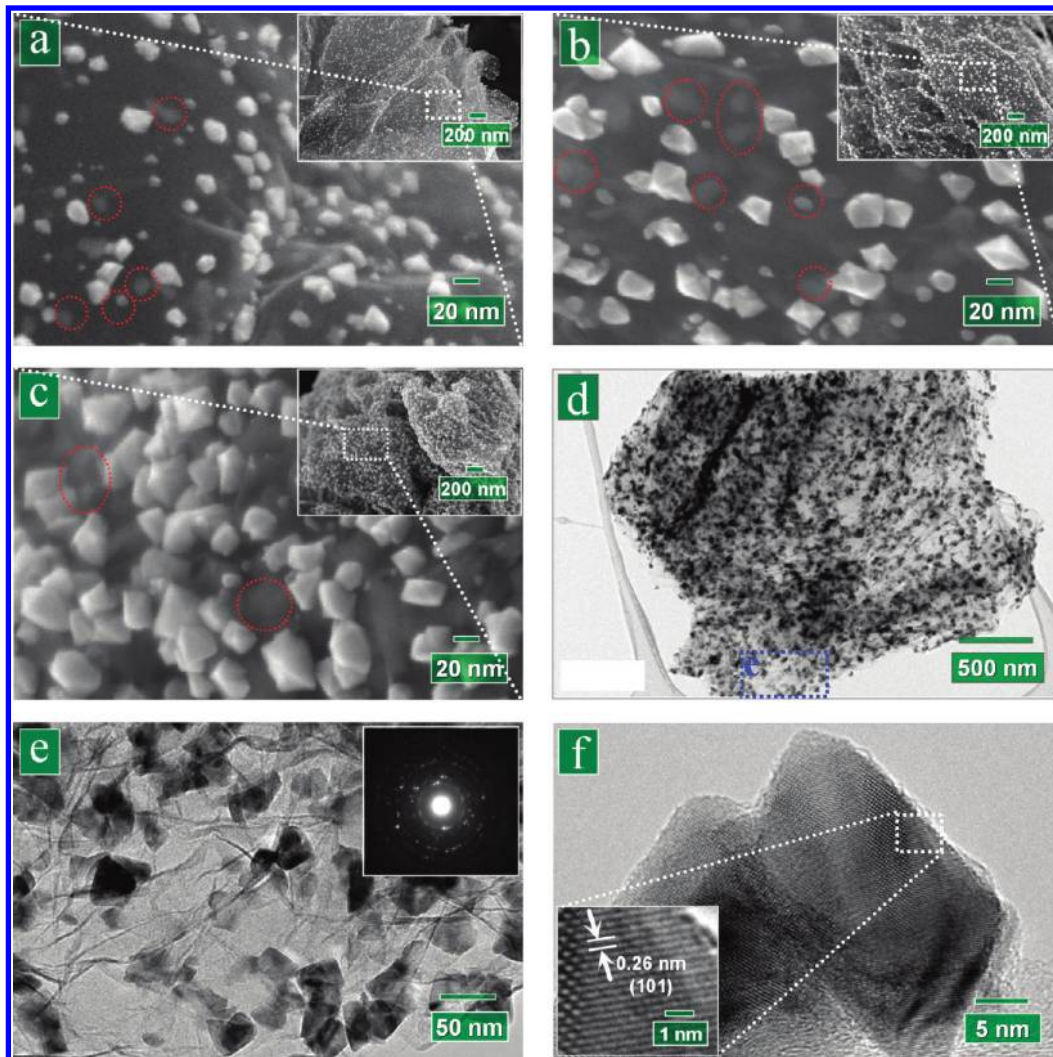


Figure 5. Crystalline SnO₂-GNS nanocomposites: (a) 100 ALD cycles of SnO₂; (b) 200 ALD cycles of SnO₂; (c) 300 ALD cycles of SnO₂; (d) low magnification TEM image of 300-cycle SnO₂; (e) and (f) HRTEM images of 300-cycle SnO₂.

and then these sites nucleated later and experienced fewer ALD-SnO₂ cycles. In particular, we observed that, besides the nanoparticles sitting on top of the graphene surface, there are also numerous nanoparticles encapsulated inside GNS, as some are red-circled in Figure 5(a)–(c). The aforementioned results have three important implications: (1) the porous structure of GNS provided space for precursors to enter and thereby to deposit; (2) GNS consisted of only a few layers of graphene were functionalized in both sides; (3) as a gas–solid reaction system, ALD can provide well-controlled deposition through adjusting the number of ALD cycles. Furthermore, the sample after 300-cycle ALD-SnO₂ was further examined using TEM. Figure 5(d) revealed similar information as Figure 5(c), and a blue-circled part marked with “e” was enlarged in Figure 5(e). Clearly we can observe the nanoparticles located on the upside and downside of GNS. The insert of Figure 5(e) disclosed that the SnO₂ nanoparticles are crystalline and were further examined by HRTEM in Figure 5(f). It was clearly shown that the SnO₂ nanoparticles are with a characteristic lattice fringe of (101). Combined with XRD spectra (Figure 2(a)), we can conclude that the SnO₂-GNS nanocomposites produced at 400 °C are with a crystalline SnO₂ component, and SnO₂ nanoparticles are tunable in size as well.

In the above-discussed results, we deduced that the ALD strategy is a facile approach to synthesize SnO₂-GNS hybrid

composites with controllable amorphous/crystalline phase as well as tunable morphologies of SnO₂ component. It is worth noting that growth temperature plays an important role in determining the structural phases of SnO₂, i.e., a low temperature contributes to amorphous phase while a high temperature is responsible for crystalline phase. Thus, it is necessary to explore the underlying mechanisms for a better understanding and manipulating the synthesis process. In this way, we explained the phenomena by applying the knowledge of surface chemistry and it is believed that surface reactions are temperature-dependent.

As stated above, ALD is a surface-controlled process. So, the initiation of an ALD process is highly dependent on the functional groups carried by pristine samples. As disclosed by FTIR spectra (Figure 2(d)), the as-synthesized GNS samples were dominantly attached with hydroxyl (–OH) groups. Thus, the hydroxyl groups guaranteed the initiation of ALD-SnO₂, as described in Reaction 2-A. To explain controllable structural phases of SnO₂, however, we noticed that the corresponding surface reactions are temperature-dependent in nature. In this way, Puurunen⁴¹ made an excellent review on ALD processes of using metal chlorides and water as the precursors, and noticed that this sort of ALD process (e.g., TiO₂, and ZrO₂) experienced a phase-transition from amorphous films to crystalline nanoparticles when a threshold temperature (300 °C) was achieved.

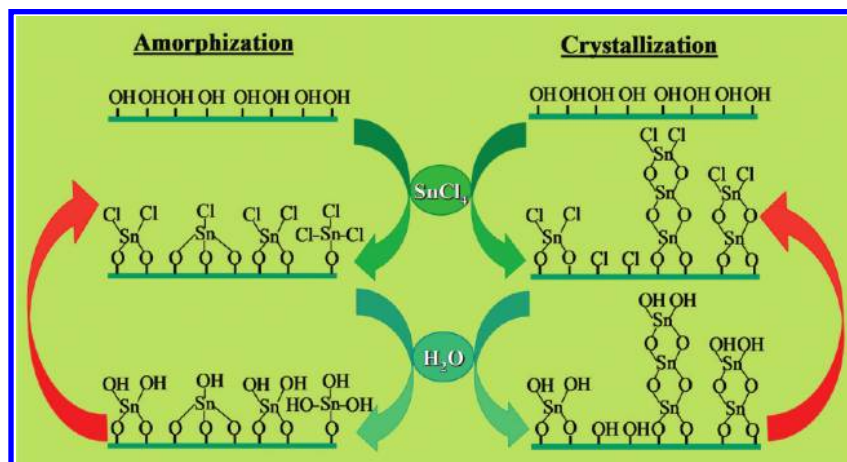
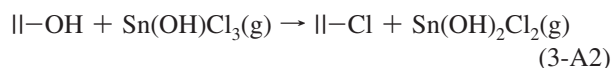
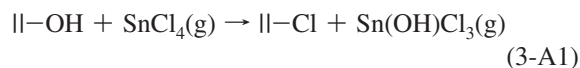
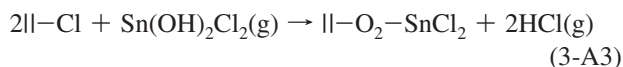


Figure 6. Schematic illustration of surface reactions occurred in ALD-SnO₂ due to different growth temperatures: (on left side) amorphization for 200 °C, and (on the right side) crystallization for 400 °C.

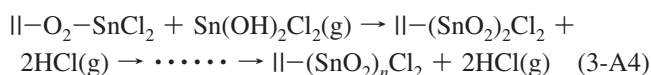
Furthermore, Puurunen proposed different underlying mechanisms for them: (a) ligand exchange (as shown in Reactions 2-A and 2-B) is the most prevalent mechanism responsible for amorphization at low temperature (<300 °C); (b) a prominent two-step chlorination in the pulse of a metal chloride is responsible for crystallization at high temperature (>300 °C). To address the two-step chlorination potentially happened in ALD-SnO₂, we proposed and described it for ALD-SnO₂ in the following reactions:



First, SnCl₄ chlorinates the surface hydroxyl groups and form an intermediate hydroxychloride molecule (Sn(OH)₂Cl₂) in two steps, as shown in Reactions 3-A1 and 3-A2. Then the hydroxychloride reacts with surface chlorine groups through its hydroxyl groups, as shown in Reaction 3-A3 as follows:



In particular, the chlorine groups on the right side of the former Reaction 3-A3 would still potentially react with hydroxychloride in a chain of reactions, as shown in the following Reaction 3-A4:



Thus, surface reactions at high temperature in a pulse of SnCl₄ could contribute a formation of multilayer. It explained why the nanoparticles grew more quickly at high temperature than at low temperature after a same number of ALD cycles. In addition, it also provided the answers to the size-varied nanoparticles and the continuously newly appeared nanoparticles with a nonlinear growth mode, for some sites might be involved in reactions in a chain (as shown in Reaction 3-A4) while others were not in a certain pulse of SnCl₄. However, the surface

reaction happened in a pulse of H₂O is still simple ligand exchange, which is the same as shown by Reaction 2-B:



To compare the differences in surface reactions incurred by different temperatures, it is believed that the half reactions occurred in the pulse of H₂O are independent of temperature, as commonly indicated by Reactions 2-B and 3-B. However, the half reactions occurred in the pulse of SnCl₄ are temperature-dependent, as described in Reaction 2-A for low temperature (200 °C) and in Reactions 3-A1 to 3-A4 for high temperature (400 °C). To further understand the different mechanisms incurred by growth temperature, we schematically illustrated the growth mechanisms in the following Figure 6. On the left side of Figure 6, surface reactions were illustrated for amorphization of deposited materials based on ligand exchange, and they are self-limiting in nature. On the right side of Figure 6 for crystallization, however, the surface reactions (as stated in above Reactions 3-A1 to 3-A4) are not self-limiting in the pulse of SnCl₄ while the ones are self-limiting in the pulse of H₂O, leading to the formation of multilayers dependent on reactive sites in one ALD cycle. In particular, as noticed by Puurunen,⁴¹ the transition between ligand exchange and chlorination might happen suddenly when the growth temperature is over a certain threshold, which is suggested around 300 °C. Obviously, it is growth temperature that influences the structural phases of deposited SnO₂ via surface chemistry.

In addition, it is noteworthy that the ALD-SnO₂ at 200 °C experienced an island-like growth in the first 200 cycles before a uniform layer was formed by coalescence of growing nanoparticles. It should be particularly clarified that the island-like growth mode at 200 °C is in essence different from the formation of crystalline SnO₂ nanoparticles at 400 °C. The island formation at 200 °C is mainly caused by the poor reactivity of the template surface⁴² and the growth mode of SnO₂ is substrate-inhibited by a lower OH group density. Thus, the growth rate is low in the beginning. However, the growth rate should be increased to a constant value while the islands coalesce into a film with increased ALD cycles. However, the formation of nanoparticles at 400 °C is not restricted by the reactivity of the template surface but due to the chlorination process in which the multilayer formation occurs.

4. Conclusions

We applied a nonaqueous ALD approach for synthesis of MO-GNCs, which was successfully exemplified with the preparation of SnO₂-GNS hybrid composites using SnCl₄ and H₂O as the ALD precursors. This strategy exhibited many unique advantages in synthesizing MO-GNCs. First of all, it is a facile vapor route, which needs no further post-treatment (such as, filtration, washing, and annealing) widely used in solution-based methods.^{15–19} Second, the ALD approach can well tune and control the deposited metal oxide on both morphologies and structural phases. As demonstrated in this work, the as-deposited SnO₂ was shown with nanoparticles/films as well as in form of amorphous/crystalline phases through adjusting the ALD cycling numbers and suitable growth temperatures. It has not been reported that both amorphous and crystalline SnO₂ have been synthesized with a single method in earlier studies. Third, this ALD approach has the potential for mass production. As reported earlier by George's group,^{43,44} ALD can be combined with fluidization technology⁴³ or rotary devices⁴⁴ for coating nanoparticles of large quantities. Thus, it is reasonable to believe that MO-GNCs can be produced in large quantities with this ALD route. Specifically, the as-synthesized SnO₂-GNS hybrid nanocomposites can be important candidates for many applications, such as Li-ion batteries,^{18–20} gas-sensing,⁴⁵ as well as solar cells.⁴⁶ The controllable amorphous/crystalline phase of SnO₂ would provide more choices for seeking a better performance of the aforementioned applications and is also potentially appealing for academic curiosity.

Acknowledgment. This research was supported by the Natural Science and Engineering Research Council of Canada (NSERC), Canada Research Chair (CRC) Program, Canadian Foundation for Innovation (CFI), Ontario Research Fund (ORF), Early Researcher Award (ERA) and the University of Western Ontario.

Supporting Information Available: SEM images for natural graphite and graphite oxide; SEM images for amorphous SnO₂-GNS nanocomposites. This material is available free of charge via the Internet at <http://pubs.acs.org>.

References and Notes

- Su, D. S.; Schlögl, R. *ChemSusChem* **2010**, *3*, 136.
- Spitalsky, Z.; Tasis, D.; Papagelis, K.; Galiotis, C. *Prog. Polym. Sci.* **2010**, *35*, 357.
- Sun, L.; Gibson, R. F.; Gordaninejad, F.; Suhr, J. *Compos. Sci. Technol.* **2009**, *69*, 2392.
- Zeng, Z.; Zhou, X.; Huang, X.; Wang, Z.; Yang, Y.; Zhang, Q.; Boey, F.; Zhang, H. *Analyst* **2010**, *135*, 1726.
- Novoselov, K. S.; Geim, A. K.; Morozov, S. V.; Jiang, D.; Zhang, Y.; Dubonos, S. V.; Grigorieva, I. V.; Firsov, A. A. *Science* **2004**, *306*, 666.
- Stankovich, S.; Dikin, D. A.; Dommett, G. H. B.; Kohlhaas, K. M.; Zimney, E. J.; Stach, E. A.; Piner, R. D.; Nguyen, S. T.; Ruoff, R. S. *Nature* **2006**, *442*, 282.
- Eda, G.; Unalan, H. E.; Rupasinghe, N.; Amaratunga, G. A. J.; Chhowalla, M. *Appl. Phys. Lett.* **2008**, *93*, 233502.
- Wei, T.; Luo, G.; Fan, Z.; Zheng, C.; Yan, J.; Yao, C.; Li, W.; Zhang, C. *Carbon* **2009**, *47*, 2290.
- Qi, X.; Pu, K.-Y.; Zhou, X.; Li, H.; Liu, B.; Boey, F.; Huang, W.; Zhang, H. *Small* **2010**, *6*, 663.
- Li, Y.; Gao, W.; Ci, L.; Wang, C.; Ajayan, P. M. *Carbon* **2010**, *48*, 1124.
- Zhou, X.; Huang, X.; Qi, X.; Wu, S.; Xue, C.; Boey, F. Y. C.; Yan, Q.; Chen, P.; Zhang, H. *J. Phys. Chem. C* **2009**, *113*, 10842.
- Guo, S.; Dong, S.; Wang, E. *ACS Nano* **2010**, *4*, 547.
- Huang, X.; Zhou, X.; Wu, S.; Wei, Y.; Qi, X.; Zhang, J.; Boey, F.; Zhang, H. *Small* **2010**, *6*, 513.
- Williams, G.; Seger, B.; Kamat, P. V. *ACS Nano* **2008**, *2*, 1487.
- Wang, D.; Choi, D.; Li, J.; Yang, Z.; Nie, Z.; Kou, R.; Hu, D.; Wang, C.; Saraf, L. V.; Zhang, J.; Aksay, I. A.; Liu, J. *ACS Nano* **2009**, *3*, 907.
- Lee, J. M.; Pyun, Y. B.; Yi, J.; Choung, J. W.; Park, W. I. *J. Phys. Chem. C* **2009**, *113*, 19134.
- Wu, J.; Shen, X.; Jiang, L.; Wang, K.; Chen, K. *Appl. Surf. Sci.* **2010**, *256*, 2826.
- Yao, J.; Shen, X.; Wang, B.; Liu, H.; Wang, G. *Electrochem. Commun.* **2009**, *11*, 1849.
- Wang, D.; Kou, R.; Choi, D.; Yang, Z.; Nie, Z.; Li, J.; Saraf, L. V.; Hu, D.; Zhang, J.; Graff, G. L.; Liu, J.; Pope, M. A.; Aksay, I. A. *ACS Nano* **2010**, *4*, 1587.
- Paek, S. M.; Yoo, E.; Honma, I. *Nano Lett.* **2009**, *9*, 72.
- George, S. M. *Chem. Rev.* **2010**, *110*, 111.
- Knez, M.; Nielsch, K.; Niinistö, L. *Adv. Mater.* **2007**, *19*, 3425.
- Kim, H.; Lee, H. B. R.; Maeng, W. J. *Thin Solid Films* **2008**, *517*, 2563.
- Li, Z.; Barry, S. T.; Gordon, R. G. *Inorg. Chem.* **2005**, *44*, 1728.
- Rosental, A.; Tarre, A.; Gerst, A.; Uustare, T.; Sammelselg, V. *Sens. Actuators, B* **2001**, *77*, 297.
- Takeuchi, T.; Shoji, K.; Tadano, T.; Doteshta, I.; Onodera, S. *Thin Solid Films* **2003**, *442*, 98.
- Rosental, A.; Tarre, A.; Gerst, A.; Sundqvist, J.; Härsta, A.; Aidla, A.; Aarik, J.; Sammelselg, V.; Uustare, T. *Sens. Actuators B* **2003**, *93*, 552.
- Du, X.; Du, Y.; George, S. M. *J. Vac. Sci. Technol. A* **2005**, *23*, 581.
- Hummers, W. S.; Offeman, R. E. *J. Am. Chem. Soc.* **1958**, *80*, 1339.
- Schniepp, H. C.; Li, J. L.; McAllister, M. J.; Sai, H.; Herrera-Alonso, M.; Adamson, D. H.; Prud'homme, R. K.; Car, R.; Saville, D. A.; Aksay, I. A. *J. Phys. Chem. B* **2006**, *110*, 8535.
- Celzard, A.; Mareche, J. F.; Furdin, G. *Prog. Mater. Sci.* **2005**, *50*, 93.
- Lee, D. W.; Santos, L. D. L.; Seo, V. J. W.; Felix, L. L.; Bustamante, A.; Cole, D. J. M.; Barnes, C. H. W. *J. Phys. Chem. B* **2010**, *114*, 5723.
- Tang, L.; Wang, Y.; Li, Y.; Feng, H.; Lu, J.; Li, J. *Adv. Funct. Mater.* **2009**, *19*, 2782.
- Chen, W.; Yan, L.; Bangal, P. R. *Carbon* **2010**, *48*, 1146.
- Singh, V. K.; Patra, M. K.; Manoth, M.; Gowd, G. S.; Vadera, S. R.; Kumar, N. *New Carbon Mater.* **2009**, *24*, 147.
- Nethravathi, C.; Nisha, T.; Ravishankar, N.; Shivakumara, C.; Rajamathi, M. *Carbon* **2009**, *47*, 2054.
- Rao, C. N. R.; Biswas, K.; Subrahmanyam, K. S.; Govindaraj, A. *J. Mater. Chem.* **2009**, *19*, 2457.
- Ferrari, A. C.; Robertson, J. *Phys. Rev. B* **2000**, *61*, 14095.
- Kudin, K. N.; Ozbas, B.; Schniepp, H. C.; Prud'homme, R. K.; Aksay, I. A.; Car, R. *Nano Lett.* **2008**, *8*, 36.
- Stankovich, S.; Dikin, D. A.; Piner, R. D.; Kohlhaas, K. A.; Kleinhammes, A.; Jia, Y.; Wu, Y.; Nguyen, S. T.; Ruoff, R. S. *Carbon* **2007**, *45*, 1558.
- Puurunen, R. L. *Chem. Vap. Deposition* **2005**, *11*, 79.
- Puurunen, R. L.; Vandervorst, W. *J. Appl. Phys.* **2004**, *96*, 7686.
- Hakim, L. F.; George, S. M.; Weimer, A. W. *Nanotechnology* **2005**, *16*, S375.
- Cavanagh, A. S.; Wilson, C. A.; Weimer, A. W.; George, S. M. *Nanotechnology* **2009**, *20*, 255602.
- Batzill, M. *Sensors* **2006**, *6*, 1345.
- Snaith, H. J.; Ducati, C. *Nano Lett.* **2010**, *10*, 1259.